PAPER

Check for updates

Morphology and property tuning in ZnO–Ni hybrid metamaterials in vertically aligned nanocomposite (VAN) form†

Nirali A. Bhatt, [ID] [a] Lizabeth Quigley,[a] Shiyu Zhou,[a] Anirutha Gnanasabai,[a] Abhijeet Choudhury,[a] Yizhi Zhang, [ID] [a] Jianan Shen,[a] Juanjuan Lu, [ID] [a] Aleem Siddiqui,[c] Raktim Sarma[cd] and Haiyan Wang [ID] *[ab]

ZnO thin films have attracted significant interest in the past decades owing to their unique wide band gap properties, piezoelectric properties, non-linearity and plasmonic properties. Recent efforts have been made in coupling ZnO with secondary phases to enhance its functionalities, such as Au–ZnO nanocomposite thin films with tunable optical and plasmonic properties. In this work, magnetic nanostructures of Ni are incorporated in ZnO thin films in a vertically aligned nanocomposite (VAN) form to couple magnetic and plasmonic response in a complex hybrid metamaterial system. Nickel (Ni) is of interest due to its ferromagnetic and plasmonic properties along with gold (Au) which is also plasmonic. Therefore, two approaches, namely, tuning of the deposition pressure and use of a ZnO–Au seeding layer have been attempted to achieve unique Ni nanostructures in addition to tuning of the microstructure. Together, both approaches demonstrate a range of microstructures such as core–shell, nanodisk, nanocup, and nanocube-like morphologies not previously attempted. Additionally, there is effective tuning of properties. Specifically, the seeding layer thickness causes hyperbolic behavior as well as redshift in the surface plasmon resonance (SPR) wavelength. The addition of the ZnO–Au seeding layer directly influences the optical properties. Plus, regardless of the different approaches, the films demonstrate magnetic anisotropy based on the composition and microstructure of the film which impacted the saturation magnetization and coercivity. This study demonstrates the potential of ZnO-based complex hybrid metamaterials with coupled electro-magneto-optical properties for integrated photonic devices.

1. Introduction

Hybrid metamaterials are a type of materials possessing properties not naturally seen in nature that are composed of multiple types of materials. Simply the morphology of the nanostructures is what controls these properties.[1] Metamaterials have many advantages such as their ability to influence light interactions,[2] and can be used in acoustics, waveguides, and sensors.[3] One such type of metamaterial thin film can be hybrid metamaterials made of oxide-metal phases. This type of thin films has the advantage of having properties resulting from the metal and the oxide. Consequently, it has

unique magnetic, optical, and electrical properties resulting from the two phases. Plus, the resultant films could present large anisotropy when grown in a way that gives an ordered nanostructure. For example, such hybrid metamaterials made in vertically aligned nanocomposites (VAN) form have shown very strong optical anisotropy, magnetic anisotropy and interface based electro-magneto-optical coupling properties.[4]

VANs are a unique type of thin film nanostructure that is comprised of a pillar in matrix form. The structure itself can be tuned in terms of strain, functionality, and properties simply based on the materials that are chosen for the system. The large anisotropy that presents in this type of nanostructure aids in the strain tuning and results in the change in properties. VAN presents an advantage in the ability to choose two or more different materials with distinct properties and create a single film that couples those properties (i.e. optical, magnetic, and electric) and creates new emergent properties not present in either material, hence a metamaterial.[5] Plus, VAN are self-assembled nucleation and growth which means that the fabrication is a relatively easy one-step growth method[6] as long as the deposition conditions which control the kinetics, surface energy, and strain are optimized.[7]

[a]School of Materials Engineering, Purdue University, West Lafayette, IN 47907, USA. E-mail: hwang00@purdue.edu

[b]School of Electrical and Computer Engineering, Purdue University, West Lafayette, IN 47907, USA

[c]Sandia National Laboratories, Albuquerque, NM 87123, USA

[d]Center for Integrated Nanotechnologies, Sandia National Laboratories, Albuquerque, NM 87123, USA

Zinc oxide (ZnO) is a well-known oxide that has been used in metal-oxide hybrid metamaterials because it is a wide band gap semiconductor, is piezoelectric, and can be a transparent conductive oxide. Due to the benefits offered by VAN, ZnO has been incorporated into VAN growth and studied. Previous ZnO-based VAN have been studied. Specifically, there is the ZnO–Au system where the oxygen background pressure and laser frequency tuning[8] were examined in addition to Au concentration variation.[9] There were also many ZnO-alloyed films like the ZnO–Au–Cu alloy and ZnO–Au–Al alloy where a seeding layer approach was used to improve the growth of these films.[10] The ZnO–Ag–Au alloy study looked at the impact of background pressure on morphology.[11] For ZnO-Oxide studies, ZnO–LSMO (lanthanum strontium manganite, $La_{0.7}Sr_{0.3}MnO_3$) is the main material system that has been explored thus far that shows VAN structure and it explored the impact of film thickness on magnetic properties and growth.[12] Additionally, all the ZnO-metal material systems explored mainly at optical property tuning with the microstructure which presents a large gap in this material system. Since Au, Cu, Al, and Ag are not ferromagnetic, there is no understanding of the magneto-optical coupling in ZnO-based VAN films.

In this work, we propose to grow a new ZnO–Ni VAN system to close the gap by using Ni, a known ferromagnetic material, to understand how the magnetic properties couple with the optical properties. Additionally, this system demonstrates the growth of Ni as a secondary phase instead of the typical dopant material that is commonly seen in prior ZnO–Ni studies.[13–16] Dopants are usually added to ZnO to tune its bandgap.[17] A secondary phase could be advantageous because the properties of the matrix material are either maintained or enhanced due to the secondary phases by strain tuning and introduction of other functionalities. Ni can also grow as NiO, under oxygen background. NiO is antiferromagnetic in bulk form and has shown to be ferromagnetic at times in nanoparticle form.[18] To achieve Ni–ZnO nanocomposite, two methods were used. The first method is based on the control of vacuum level. The second method employs a thin ZnO–Au seeding layer that was deposited before the ZnO–Ni film of interest. These methods are selected based on the impacts of both deposition pressure and seeding layers. Specifically, the vacuum level of thin film growth, usually in the range of 10^{-7} to 10^{-10} Torr, plays an important role in the mean free path of the adatoms and the impurity level of the film. A seed layer on the other hand, is a thin film layer grown underneath the main film of interest considering its ability to reduce strain, improve crystallinity[19] and nucleation[20] of the film grown above it, enhance properties,[21] or aid in the growth of the film of interest. Fig. 1 shows the proposed films that will be discussed in this paper. Fig. 1a is the ZnO–Ni film grown in a high vacuum (2.1×10^{-6} Torr) which will be referred to as HVZN in this paper. Fig. 1b and c show the thin seeding layer and ZnO–Ni film, and a thick seeding layer and ZnO–Ni film, which will be referred to as 10ZA50ZN and 50ZA80ZN, respectively. Additionally, a low vacuum ZnO–Ni film grown at 7.4×10^{-6} Torr is shown in Fig. S1† which will be referred to as LVZN. We aim to achieve tunable ZnO–Ni nanostructures with tailorable optical and
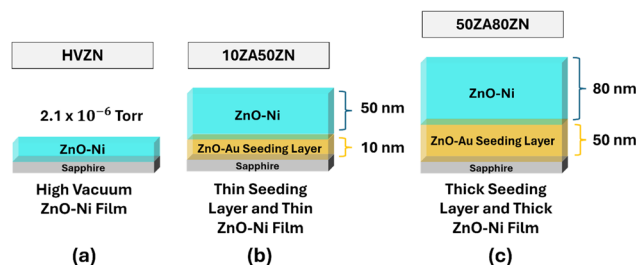

Fig. 1 Proposed thin films growths which include (a) the growth of a ZnO−Ni thin film on sapphire grown in a high vacuum environment, (b) the use of a 10 nm ZnO−Au seeding layer grown beneath 50 nm of ZnO−Ni, and (c) the use of a 50 nm ZnO−Au seeding layer grown beneath 80 nm of ZnO−Ni.

magnetic properties that could find unique applications in photonics, spintronics and other device structures.

2. Materials and methods

2.1 Thin film growth

The ZnO (70 mol%)–Ni (30 mol%) thin films including those with the ZnO plus 30 mol% Au seeding layer were deposited and grown using the pulsed laser deposition (PLD) method. All films were deposited on c-cut sapphire substrates with a KrF excimer laser ($\lambda = 248$ nm) using different targets: (1) ZnO(70% mol)–Ni(30% mol) composite target and a (2) ZnO plus 30% mol Au composite target which was only used for the films with the seeding layer approach. All the targets were made using the spark plasma sintering process. For all the films discussed, the target–substrate distance was 4.5 cm, the laser frequency of 5 Hz, and a laser energy of 420 mJ were used. For HVZN, the vacuum pressure was 2.1×10^{-6} Torr and temperature was 620 °C. For LVZN, the vacuum pressure was 7.4×10^{-6} Torr and temperature was 620 °C. For 10ZA50ZN and 50ZA80ZN, the ZnO–Au was grown at 610 °C and the ZnO–Ni was grown at 650 °C.

2.2 Microstructure characterization

The microstructure characterization in this paper was performed using X-ray diffraction (XRD), transmission electron microscopy (TEM), scanning transmission electron microscopy (STEM), and energy-dispersive X-ray spectroscopy (EDS). A Malvern PANalytical Empyrean X-ray diffractometer (XRD) from Worcestershire, UK was used to conduct θ–2θ scans with Cu K$_\alpha$ ($\lambda = 0.154$ nm) radiation. The ThermoFisher TALOS F200X TEM was utilized to get the TEM/STEM/EDS-mapping images. The cross-section TEM samples were prepared by a standard sample preparation procedure consisting of manual grinding, dimple polishing, and ion milling (PIPS 695 system, 5 keV).

2.3 Optical measurements

Optical measurements were obtained using a J.A. Woollam RC2 spectroscopic ellipsometer for ellipsometry measurements. A B-spline model coupled with a uniaxial model were applied to get optical permittivity measurements in the range of 210–2500 nm.

A Lambda 1050 UV-vis spectrophotometer was used for transmittance (% *T*) measurements.

2.4 Magnetic measurements

Magnetometry data was collected using the MPMS-3 EverCool SQUID magnetometer in the user facility of the Birck Nanotechnology Center at Purdue University, see **http://birck.research.purdue.edu**. Both the parallel and perpendicular directions were tested with the applied field and the scan was done at both 10 K and 300 K temperatures.

3. Results

3.1 Crystallinity of the ZnO–VAN films

First, X-ray diffraction was conducted to understand the crystallinity of the films. Fig. 2 presents the XRD of the θ–2θ scans of three films discussed in Fig. 1. All films were grown on c-cut sapphire. Fig. 2a shows the XRD of HVZN which demonstrates the lack of textured growth of ZnO (0002) on the substrate and instead shows ZnO (10−11). It is typical for ZnO (0002) to grow on c-cut sapphire because it is the preferred plane orientation considering the lattice matching between ZnO and c-cut sapphire.[22] However, ZnO (0002) is not seen in this sample. Instead, the lower surface energy plane of ZnO (10−11) is seen in this case. Interestingly, such preferred ZnO (10−11) growth has been reported in a study by Vijayalakshmi *et al.* using sputtering.[23] The authors concluded that the deposition time impacted on the intensity of the ZnO (10−11) peak.[23] Plus, HVZN is the only sample where the NiO(111) and Ni(111) peaks

have relatively high intensity rather than an inverse relationship as discussed in the other 2 samples below. Specifically, the Ni grows both as NiO (111) and Ni (111) though the NiO peak intensity is higher than that of Ni.

Fig. S1b† shows the XRD for the LVZN film grown at 7.4 × 10⁻⁶ Torr which shows epitaxial growth of ZnO (0002), NiO(111), and Ni (111) on c-Al₂O₃ (0006). This relationship works to explain the connection between the hexagonal wurtzite structure of the ZnO and the cubic Ni and NiO. Since Ni has a face-centered cubic crystal structure, the Ni rotates to be in the (111) to match its 3-fold symmetry with the 6-fold symmetry of hexagonal substrate and matrix.[8,9] It shows clearly textured growth. Plus, there is a peak of both ZnO(101)/NiO(111) suggesting a strain coupling and co-growth of these two phases in the thin film which will be explained by the detailed microstructure analysis in the next section.

Fig. 2b shows the XRD for 10ZA50ZN while Fig. 2c shows the XRD for 50ZA80ZN. Clearly, both films show epitaxial growth of ZnO (0002), NiO(111), Au(111), and Ni(111) on the c-cut sapphire substrate. Fig. 2b shows that there is a more prominent Ni (111) peak as compared to the NiO(111) while in Fig. 2c there is the inverse with a more prominent NiO(111) peak as compared to Ni(111). Clearly, the ZnO–Au seeding layer aids in the growth of epitaxial ZnO, Au, and Ni onto the substrate.

The seeding layer thickness could influence the crystallographic orientation and phase distribution and thus is explored. The seeding layer thickness in the aforementioned samples is about 10 nm and 50 nm for the 10ZA50ZN and 50ZA80ZN samples, respectively. First, for the 10ZA50ZN sample, the seeding layer thickness is too thin that the Au, though Au(111), is not affecting the crystallographic nature of the ZnO–Ni growth on top. That is why the Ni(111) peak is comparable to what is seen in HVZN. There is a minor NiO(111) peak that could be explained by the small strain introduced by the thin seeding layer that causes Ni to grow as NiO(111) to accommodate the strain. Furthermore, for the thick seeding layer sample, 50ZA80ZN, there is a different phase distribution induced in the film. The 50 nm ZnO–Au layer results in the formation of well-defined Au particles as will be discussed in more detail with the microstructure next. In short, the aid of the Au (111) nanoparticles allows for nucleation of the NiO(111) which is the main phase of Ni that forms due to the ZnO co-growth and interface interactions.

3.2 Microstructure characterization

The cross-section microstructure of these films was also characterized using TEM, STEM, and EDS to better understand the growth quality and film morphologies based on the different growth conditions. Fig. 3a–e presents the schematic, STEM, and EDS for HVZN. From Fig. 3b, the STEM shows cubelike VAN which is the Ni seen in Fig. 3c. Clearly, the ZnO is the matrix material as seen in Fig. 3d. The relatively low intensity could be related to the ion milling damage during sample preparation. Regardless, by comparing Fig. 3c and d, there is no interdiffusion between the ZnO and Ni. The thickness of the ZnO–Ni film is ∼20 nm.

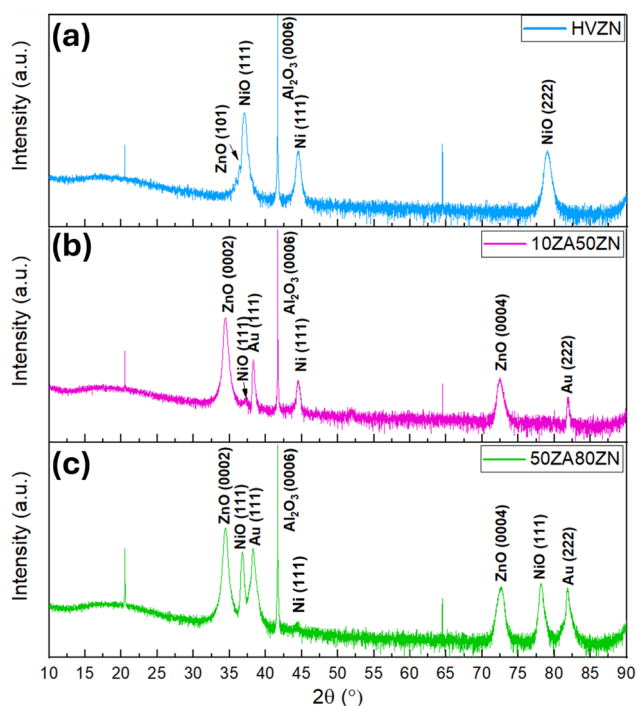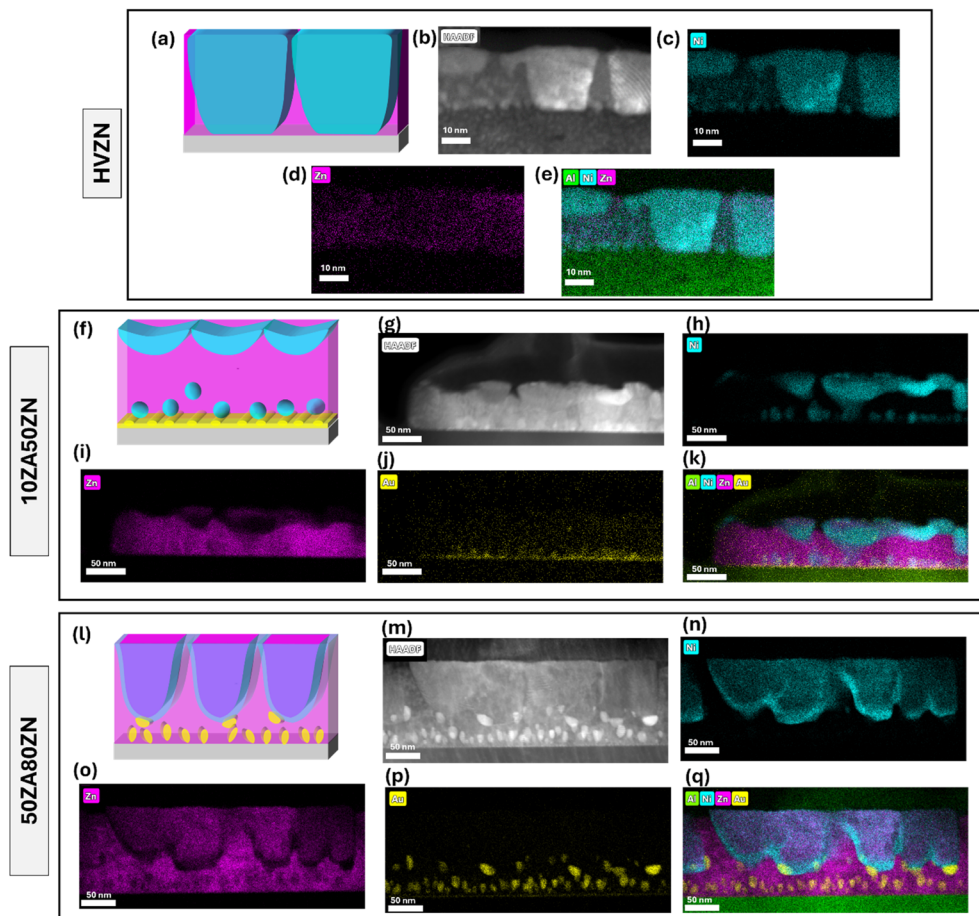**Fig. 2** XRD θ–2θ scans for the (a) high vacuum sample, (b) thin seeding layer and thin film layer sample, and (c) thicker seeding layer and thin film layer sample.

Fig. 3 Microstructure characterization of the samples. (a) Schematic drawing of the ZnO–Ni film grown in high vacuum environment. (b) Cross-section STEM and (c) EDS mapping of Ni, (d) Zn, and (e) combined Al, Ni, and Zn of the film grown in high vacuum environment. (f) Schematic drawing of the thin seeding layer and ZnO–Ni film. (g) Cross-section STEM and (h) EDS mapping of Ni, (i) Zn, (j) Au, and (k) combined Al, Ni, Zn, and Au of the thin seeding layer and ZnO–Ni film. (l) Schematic drawing of the thick seeding layer and ZnO–Ni film. (m) Cross-section STEM and (n) EDS mapping of Ni, (o) Zn, (p) Au, and (q) combined Al, Ni, Zn, and Au of the thick seeding layer and ZnO–Ni film.

In contrast, LVZN in Fig. S2† shows obvious vertical growth of Ni with the ZnO growing along with Ni with a thickness of ~40 nm. This suggests a ZnO core and NiO shell structure that has been verified in Fig. S7† from a line scan. This microstructure supports the results shown in XRD. Due to the Ni growing where the ZnO grows, the more prominent NiO peak is justifiable. Additionally, the combined ZnO and NiO peak are supported by the core–shell structure. The lack of core–shell growth in the high vacuum film supports the greater intensity Ni(111) peak seen in the XRD. The core–shell seen in LVZN and the cube-like Ni growth in HVZN is due to those microstructures having the lowest energy in the system.[24] It is surprising, however, that LVZN demonstrated a better epitaxial growth of ZnO(0002) while HVZN did not. This is counter-intuitive since typically high-quality epitaxy requires high vacuum growth.

The two samples with thin and thick seeding layer are shown in Fig. 3f–k for the thin seed layer sample 10ZA50ZN. For 10ZA50ZN, the Ni nucleates at the film–substrate interface as small particles in addition to a 'nanodisk' structure. The ZnO is present as the matrix material and the ZnO–Ni film has a thickness of 50 nm. The Au that is present due to the ZnO–Au

seeding layer is only seen at the bottom of the film due to the very thin layer. The Au mostly looks like clusters that are not big enough to be defined as nanoparticles. It is also clear that the Ni grows where there is less ZnO shown. This explains the prominent Ni peak in the XRD as well as the very low intensity NiO.

For 50ZA80ZN (Fig. 3l–q), the Au grows as well-formed particles in Fig. 3p due to the thicker layer. Unlike the thinner seeding layer seen in Fig. 3j, the Au in 50ZA80ZN grows as particles that are slightly elongated vertically like a 'pill' shape. The seeding layer in this film has a thickness of 50 nm, five times that of the thin layer in Fig. 3j. This increased thickness is what leads to this better formation of Au particles. Additionally, there is a unique Ni 'nanocup' structure that only nucleates where an Au nanoparticle is present. Interestingly, through the EDS mapping of the Ni (Fig. 3n) and Zn (Fig. 3o), it is clear that the Ni growth is accompanied by ZnO. There is a clear interface in the "nanocup" where the Ni meets the ZnO. This could mean there is a possible core–shell structure.

Because of this interesting 'nanocup' structure, plan-view TEM/STEM images were taken and Fig. S8† shows the plan-view STEM images of 50ZA80ZN. Interestingly, from the

HAADF STEM seen in Fig. S8a,† the film is made up of multiple domains which was not expected considering the highly textured growth seen in XRD. Ni (Fig. S8b†) is the major composition in the different domains that are not well connected. These Ni domains are filled by ZnO as seen in Fig. S8c.† The intensity of Au varies as typical plan-view samples have a variation in thickness. Regardless, there are Au particles. From the combined EDS map in Fig. S8e,† it is noted that at the edges of the grains it shows a darker blue suggesting that there is a greater concentration of Ni. This overall plan-view structure confirms the effects of Au seeding evidenced from the cross-section images seen in Fig. 3. The Ni nucleates only where there is a well-formed Au nanoparticle.

To better understand the change in composition of these films, Table S1† is included in the supplementary. The LVZN film (Table S1a†) has about 58%Zn and 42%Ni atomic fraction while for HVZN (Table S1b†) these change to about 6%Zn and 94%Ni. For the seeding layer films, the atomic fraction of Ni is more comparable, with ∼36% for 10ZA50ZN and ∼30% for 50ZA80ZN. Similarly, the Zn atomic fraction is ∼62% for 10ZA50ZN and ∼67% for 50ZA80ZN. The Au atomic fraction goes from 0.71% in 10ZA50ZN to 2.64% in 50ZA80ZN. It is clear that the pressure and seeding layer thickness varies the composition of the films.

This microstructure explains the higher intensity NiO peak in the XRD since the Ni is growing with the oxygen due to the ZnO core in the Ni 'nanocup'. The thickness of the ZnO–Ni film is 80 nm. It is clearly noted that the growth of a thicker ZnO–Au seeding layer leads to well defined Au nanoparticles which aid in the nucleation of the Ni into the unique 'nanocup' structures.

Additionally, it is important to note that very little to no inter-diffusion was seen at the ZnO–Ni interface for the four samples discussed. Paldi *et al.* in their study of ZnO-based nano-composites observed similar pillar in matrix morphology with minimal interdiffusion at the ZnO–metal interfaces.[25] The LVZN sample shows slight inter-diffusion of the ZnO core into the Ni shell but that could be caused by the higher-pressure environment. Unlike copper (Cu) which inter-diffuses easily with oxides and can diffusion along phase boundaries,[25,26] Ni does not diffuse as easily as that of Cu. One possible reason is related to relatively high melting temperature of Ni, $T_m = 1455$ °C, and relative inertness with ZnO and other oxides. Successfully Ni-based VAN growth has been reported in CeO_2–Ni VAN[27] and Ni–BZY VAN.[28] Regardless, interdiffusion can cause issues in thin film performance and integrity and has been shown to be eliminated if there are secondary phases at the grain boundaries.[29]

Vacuum pressure plays an important role in the deposition of the film because it not only affects what adatom species arrive at the substrate surface but also during the laser–target inter-action. The pressure during deposition determines the plume dynamics and therefore the kinetic energy and mean free path of the species that are ablated from the target.[30] Plus, the level of vacuum will also affect the uniformity and purity of the films.[30] The deposition rate also corresponds to the vacuum pressure.[31] So, when the film is grown in high vacuum (low pressure), such as the case of HVZN, the plume is highly directional.

Conversely, the plume in a high pressure (low vacuum) environment grows spherically due to more scattering with gas molecules.[32] Therefore, it is reasonable to believe that the more directional plume for the HVZN sample resulted in the nucleation of ZnO matrix and Ni nanostructure as opposed to what was seen in LVZN.

3.3 Optical properties

Considering versatile morphologies and structures observed in the Ni–ZnO nanostructures and their potential impacts on the optical responses, detailed optical characterization including UV-Vis transmittance and ellipsometry measurements were conducted considering the surface plasmon resonance (SPR) properties of Ni and Au and possible hyperbolic behavior due to the dielectric and metal in the films. Fig. 4a shows the real part of the permittivity for the HVZN (blue), 10ZA50ZN (pink), and 50ZA80ZN (green) based on the ellipsometry data collected for wavelength ranging from 650–2500 nm. The dotted lines are the real part of the permittivity in plane ($\varepsilon_\parallel$) while the solid line is the real part of the permittivity out of plane ($\varepsilon_\perp$). It is observed that both HVZN and 10ZA50ZN have positive dielectric permittivity which can be explained by the greater amount of oxide in the overall films. 50ZA80ZN on the other hand shows hyperbolic behavior for all wavelengths due to the large amount of anisotropic structures in the film and the well-defined Au nanoparticles and Ni nanocups. The out of plane real permittivity value is negative due to the Ni and Au growing out of plane in the sample. 50ZA80ZN is a Type I hyperbolic (shown as, isometrically, a hyperboloid of one sheet) structure meaning that it behaves like a metal out-of-plane and a dielectric in-plane for the entire range of wavelengths, thus making it a hyperbolic metamaterial.

Additionally, the measured reflection intensity spectra as a function of wavelength for various reflection angles is included in Fig. S3.† For all samples, the 30° angle has the lowest reflection intensity and it increases as the angle increases. From the reflection intensity, the relation to SPR phenomena can be understood since the p-polarized light is what excites the plasmons. This is why reflection intensity measured by ellipsometry is needed. Overall, since SPR results in a dip in reflection intensity since light energy is transported to the electrons in the thin film,[33] a dip in the reflection intensity is expected. Therefore, the only sample that shows this dip is seen in Fig. S3c† for the 50ZA80ZN sample at ∼620 nm. This is due to the well-defined Au nanoparticles that are not present in any of the other films. Even the thin seeding layer film (10ZA50ZN) does not demonstrate this behavior because the ZnO–Au seeding layer is too thin for the p-polarized light to excite the plasmons in the sample. Ni does not possess as strong a plasmonic response as Au, that is why HVZN and LVZN do not show the large dip in reflection intensity.

The imaginary permittivity of all samples is shown in Fig. 4b and it describes the absorption losses. The 3 samples show relatively low losses and the out of plane imaginary permittivity is the highest for the thick seeding layer sample. This can be explained by SPR phenomena seen in Fig. 4c.
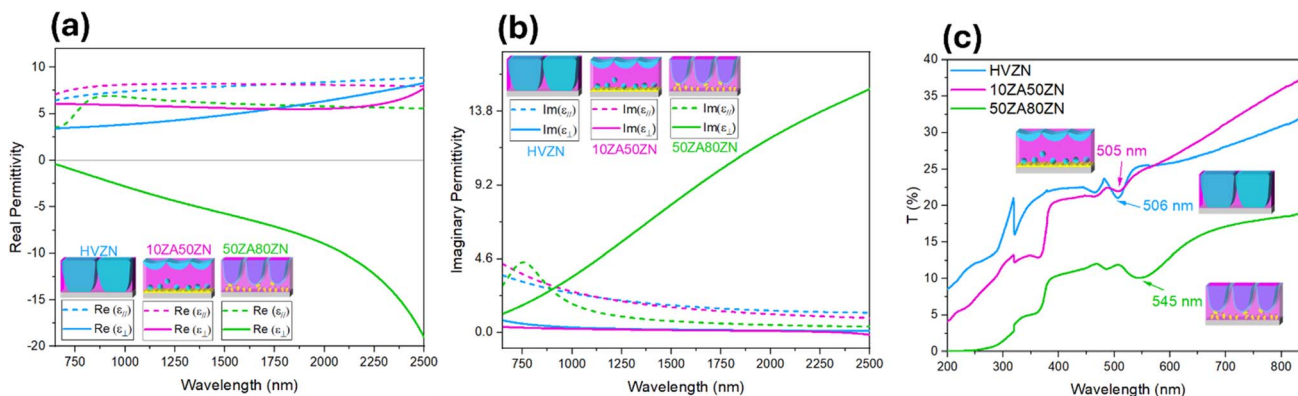
Fig. 4 (a) Real part of the optical permittivity for the 3 films discussed. The blue lines are that of the high vacuum film sample, the pink lines are that of the thin seeding layer and film sample, and the green lines are for the thick seeding layer and film sample. The dotted lines are the real part in plane while the solid line is that real part out of plane. (b) Imaginary part of the optical permittivity for the 3 films discussed. The line colors and type of line represent the same as that for (a) but for the imaginary part. (c) UV-Vis transmission (% T) of the 3 different ZnO–Ni films. The numerical values labeled on the plot represent the wavelength at which the surface plasmon resonance phenomena (SPR) is present in the films.

The real permittivity of LVZN seen in Fig. S4a† shows optical anisotropy and the film behaves overall as a dielectric, (*i.e.*, real permittivity is positive in the measured wavelength range). It is observed that the film is anisotropic throughout all wavelengths, and this can be attributed to the highly anisotropic ZnO-core and Ni-shell structure. Though anisotropic, the film behaves like a dielectric in both the in-plane and out of plane directions because of the ZnO matrix and the coupling of the ZnO and NiO in the core–shell structure as explained by the XRD above. The imaginary part of the permittivity seen in Fig. S4b† is also low, thus having low losses for this sample as well as the other three. Plus, the out of plane imaginary permittivity becomes negative at 1429 nm which for metamaterials has been shown to be an inherent property resulting from the magnetoelectric coupling effect.[34]

The UV-Vis transmittance results are shown in Fig. 4c for all three samples. The property of interest was the surface plasmon resonance (SPR) which could show as a dip in the data where the frequency of light is absorbed if it matches that of the frequency of the metal electrons in the film. The SPR wavelength for HVZN is 506 nm. The SPR wavelength for 10ZA50ZN is 505 nm and it jumps to 545 nm with 50ZA80ZN. This large redshift could be attributed to the Au presence in the film. A previous study which used the same concentration ZnO–Au film reported the same SPR wavelength as seen in 50ZA80ZN.[9] Additionally, since SPR is related to the absorption of light, the larger out of plane imaginary permittivity of 50ZA80ZN seen in Fig. 4b can be explained by this phenomenon and of course the out of plane anisotropy resulting from the metals. As mentioned above, the imaginary permittivity is related to the SPR and can lead to a broadening of the SPR peak[35] which is seen for 50ZA80ZN and explains the out of plane imaginary permittivity for this sample.

The well-defined Au particles that are present in the thicker seeding layer film can be attributed to this prominent jump in SPR. Plus, there is a broadening of the absorption edge that can also be attributed to the Au particles since they are very small in the thinner seeding layer but become elongated particles with

more defined aspect ratios which has been shown to impact the SPR.[36] The % T decreases when the seeding layer grows thicker meaning less light passes through the film due to the greater metal content from both the Ni and Au. Overall, it is apparent that the thicker ZnO–Au seeding layer drastically changes the permittivity and SPR properties of these ZnO–Ni thin films. The thicker seeding layer demonstrates hyperbolic behavior which is representative of metamaterials which have the ability to be used in many different applications such as photovoltaic devices and hyperlenses.[37] Additionally, the SPR change demonstrates tunability simply based on the thickness of the ZnO–Au seeding layer. This tuning can be utilized in applications such as sensors. Au is an important material used for SPR. Future research could grow the seeding layer with different concentrations of Au or different thicknesses. Fig. S4c† shows the transmittance plot of Sample 4 with an absorption valley at 505 nm, just as that seen in Sample 2.

The bandgap was calculated using the transmittance data and applying the Tauc plot method which is seen in Fig. S5† for all samples. Both HVZN and 10ZA50ZN have comparable bandgaps of 3.49 eV and 3.46 eV (Fig. S5a and S5b†). 50ZA80ZN seen in Fig. S5c† has a bandgap of 3.58 eV while the bandgap of LVZN increases to 4.41 eV (Fig. S5d†). Clearly, varying nanostructures in these films leads to this change in bandgap. Since LVZN demonstrates the core–shell pillar structure, it differs from the other films because the interface between the ZnO core and NiO shell can impact the strain and therefore the electronic structure. This is a possible reason for the larger bandgap observed in LVZN than the other films.

3.4 Magnetic properties

Ni is not only a plasmonic metal but also exhibits ferromagnetic properties. NiO is antiferromagnetic but nanostructured NiO has been reported as ferromagnetic. In addition, the change in microstructure could impact the magnetic properties of the films. Magnetic measurements including saturation magnetization and coercivity were taken. Fig. 5a and b show the M–H
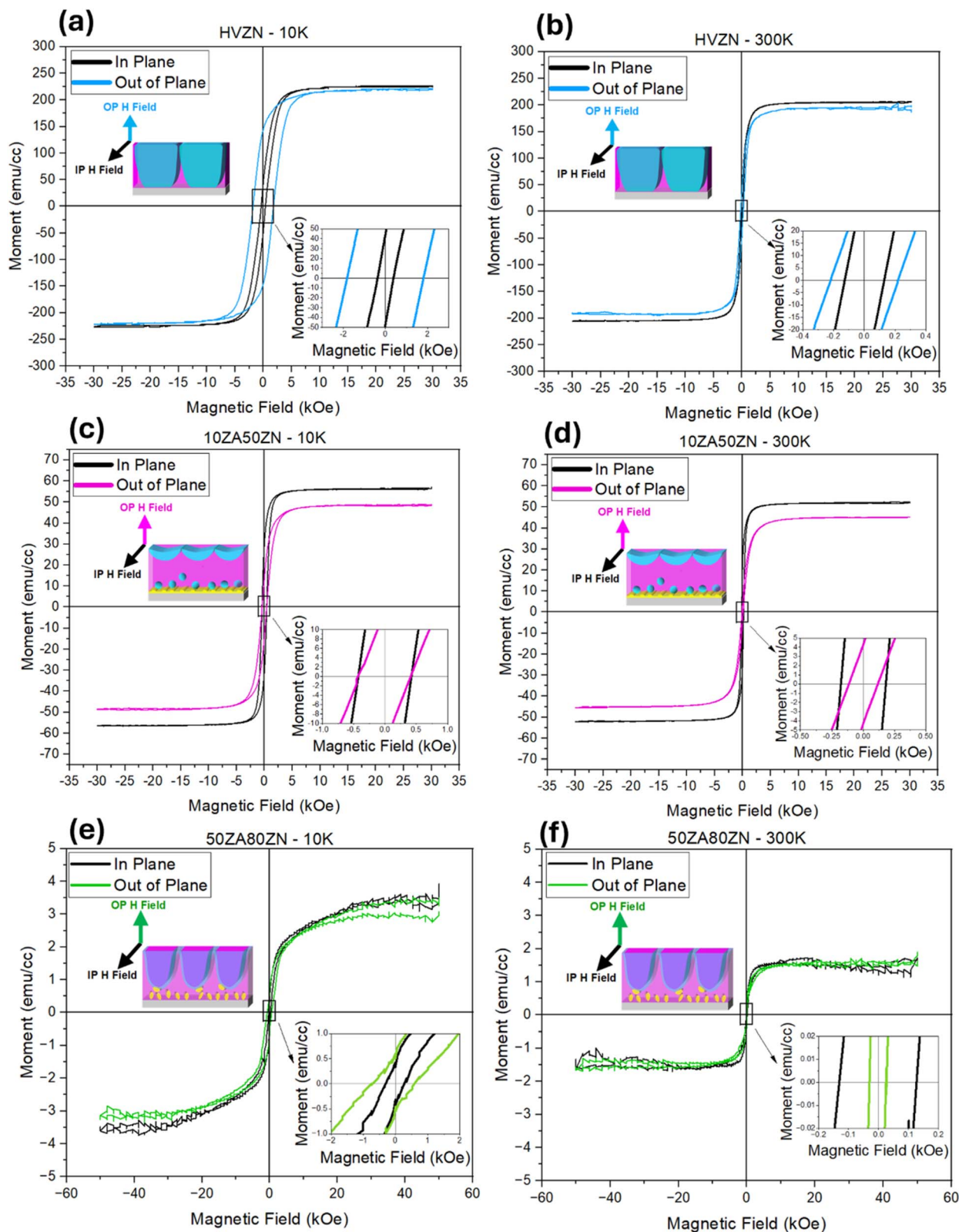
Fig. 5 Magnetic data of magnetic moment *versus* magnetic field for the high vacuum thin film at (a) 10 K and (b) 300 K. Magnetic moment *versus* magnetic field for the thin seeding layer and film at (c) 10 K and (d) 300 K. Magnetic moment *versus* magnetic field for the thick seeding layer and film at (e) 10 K and (f) 300 K. All plots have an inset that magnifies the hysteresis loop near 0 emu cm^{-3} magnetic moment and 0 kOe.

loops for HVZN grown at high vacuum taken at 10 K and 300 K, respectively. Clearly, the saturation magnetization is comparable for both the in-plane (IP) and out-of-plane (OP) at each measured temperature. However, the coercivity of the 10 K measurement seen in Fig. 5a is greater for the OP direction than that of the IP. This differs from the 300 K measurement seen in Fig. 5b where the IP and OP are comparable. To understand these results, the microstructure can be correlated. Since the Ni growth is 'cube-like', the aspect ratio of the growth is close to 1 meaning the Ni distribution in IP and OP direction is similar leading to the minor magnetic anisotropy. The improved coercivity for the 10 K measurement simply results from low temperature reducing the thermal energy, thus making it harder to switch the magnetic moments.[38]

Fig. S6a and S6b† demonstrate magnetic properties of the low vacuum film (LVZN). The film is magnetically anisotropic regardless of temperature due to the different loop shapes of the OP and IP measurements. Plus, the saturation magnetization for the OP is clearly greater than that of the IP with the coercivity being about the same regardless of temperature. This large anisotropy for both temperatures likely arises from the gaps in between the ZnO core and Ni shell structure as seen by the black areas in Fig. S2e.† Additionally, there is a clear shape anisotropy resulting from the OP growth of the Ni shell while the ZnO grows more IP. The aspect ratio of the Ni growth is contributing greatly to the OP anisotropy.

The magnetic properties of Ni is relatively weak as compared to Fe, because of its nearly full 3d orbital.[39] Furthermore, magnetic domains are the cause of the ferromagnetic property observed in Ni.[40] The thin films deposited under different vacuum pressure (i.e., HVZN and LVZN), however, are grown in nanometer length scales making their atomic magnetic moments and magnetic anisotropy behave differently than just bulk Ni. Additionally, exchange interactions which are the coupling of atomic or molecular magnetic moments between the different materials in thin films are also necessary to observe ferromagnetic behavior.[40] With that being said, the difference in hysteresis between HVZN and LVZN is a direct result of the shape anisotropy in the individual films. Consequently, this impacts the coercivity. As the name suggests, shape anisotropy is dependent on the shape of the magnetic nanostructures and the axis on which they magnetize easily. Therefore, it is reasonable that the LVZN sample, which has a high aspect ratio core–shell structure with the Ni and NiO growing out of plane, to have large magnetic anisotropy between the in-plane and out-of-plane directions. HVZN on the other hand does not have a high aspect ratio Ni or NiO structure and therefore the magnetic anisotropy is less obvious. This is a reason why the coercivity is less for LVZN in the out-of-plane direction since the hard axis magnetizes easily due to dipole–dipole interactions. HVZN on the other hand, has larger coercivity both in-plane and out-of-plane because of the greater presence of Ni(111) than that in LVZN.

Although the ZnO–Au seeding layer is not composed of materials known to have prominent magnetic properties, the growth of the seeding layer before the ZnO–Ni film could add to the anisotropy and change the magnetic properties of the films

by affecting the ZnO–Ni microstructure. Fig. 5c and d show the magnetic properties data for the film with the thinner ZnO–Au seeding layer (10ZA50ZN) at both 10 K and 300 K respectively. The film is magnetically anisotropic and has low coercivity and higher saturation magnetization for both temperatures. Fig. 5e and f show the magnetic data for the film with the thicker ZnO–Au seeding layer (50ZA80ZN) at 10 K and 300 K respectively. This film has low coercivity and lower saturation magnetization when compared to the thinner seeding layer film.

In order to understand why 10ZA50ZN and 50ZA80ZN show these properties, it is important to understand the microstructure. Bulk ZnO and Au are reported to be diamagnetic[41,42] while bulk Ni is ferromagnetic, and bulk NiO is antiferromagnetic.[43] However, the Au, Ni, and NiO present in these films grow with unique nanostructures which can impact the magnetic properties. The thinner seeding layer film has shown to grow more Ni (111) than NiO (111) through XRD measurements aiding to the improved saturation magnetization. 50ZA80ZN shows the lowest saturation magnetization due to the Au and NiO in the sample which would lower the amount of magnetization that can be achieved in the sample. Saturation magnetization can be influenced by microstructure, atomic structure, and magnetic interactions[44] which explains why each sample behaves the way it does magnetically.

Furthermore, the composition of the films, as discussed previously and seen in Table S1† plays a role in the magnetic properties. As the Ni composition changes, so does the magnetic moments of the films. This is due to the plume kinetics in different vacuum environments.

It is clear that all 3 film samples are soft magnetic thin films due to their extremely thin hysteresis loops characterized by high saturation magnetization and low coercivity.[45] This could be a result of the contribution of more Au and NiO.

3.5 Discussion

There have been few other studies that explored ZnO–Ni thin film growth. One such study grew ZnO–Ni VAN to understand its possible applications for magneto-acoustic materials.[25] Though the growth was done in vacuum on c-cut sapphire substrate, with a 30% mol Ni concentration ZnO–Ni composite target, minor NiO_x oxide peaks were present in the XRD scans which were not seen in any of the previous films in this study. Plus, the Ni growth was most like similar to the film grown under high vacuum (HVZN) seen in Fig. 2b. However, the morphology is different with a wider width than height. The main reason for this difference could be a result of the different growth temperatures –500 °C versus 620 °C. The lower temperature in the magneto-acoustic study perhaps impacts on the diffusion mechanisms and resulted in the slightly varied growth.

Interestingly, the microstructure seen in HVZN more closely resembled the Ni growth in the combinatorial growth study of LSMO-NiO grown on STO substrates.[46] One of the main differences is the use of two separate targets, a NiO target and an LSMO target. In this study, a composite target of ZnO–Ni was used which deposits Ni and ZnO simultaneously on the substrate. A combinatorial growth process in an oxygen

background with annealing was used with the LSMO–NiO which allowed for the cubelike growth of the Ni in the LSMO matrix. Plus, this combinatorial approach would be an interesting method to recreate with the ZnO–Ni to see if the same Ni microstructure results.

Overall, this work gives a better understanding of the ZnO–Ni system by investigating it from different growth background pressures and seeding layer. With the change in vacuum condition and the growth of a seeding layer to aid in the growth of the ZnO–Ni film, there were new insights into the growth and properties of the films. First, it was shown that a ZnO–Au seeding layer can be utilized to achieve epitaxial growth of ZnO–Ni. Not only did this improve film growth but incorporated plasmonic properties which aid in making the nanocomposites metamaterials. Second, it was seen that the vacuum level impacts the microstructure drastically. The higher vacuum ZnO–Ni film grew more cube-like and not epitaxially while the lower vacuum ZnO–Ni grew as core–shell and epitaxially. Plus, the core–shell growth was achieved through a single step growth and a composite target. Lastly, there was tuning of the optical properties because of the thickness variation of the seeding layer. Clear hyperbolic behavior resulted as the seeding layer thickness increased because it improves the ZnO–Ni microstructure. Future directions for this work include the need to understand why lower vacuum results in epitaxial growth of ZnO while higher vacuum does not. Perhaps, trying a wider range of vacuum pressure on ZnO–Ni growth could provide a better understanding of how the microstructure could vary and in turn, the growth quality. Clearly, the ZnO, Ni, and Au provide a unique mix of properties such as plasmonic and ferromagnetic, which make these metamaterial thin films good candidates for optoelectronic devices, sensors, and data storage applications.

4. Conclusion

In this work, ZnO–Ni films were grown and analyzed under different growth conditions. First, the level of vacuum was varied and second, a ZnO–Au seeding layer was incorporated to aid the ZnO–Ni growth. The level of vacuum greatly impacted the microstructure, going from a cube-like Ni growth to a core–shell as the vacuum went from high to low. On the other hand, as the seeding layer thickness increases, the Ni nanostructures vary from nanodisk to nanocup structure. The Au microstructure grew as nanoparticles in the thick seeding layer sample and interestingly, Au aided in the nanocup nucleation because of its presence below each nanocup. Optically, the only sample that demonstrated hyperbolic behavior was the one with the well-defined Au particles in the thick seeding layer sample. All samples behaved as soft magnetic materials with the cube-like Ni sample grown under high vacuum having the largest coercivity when measured at 10 K. Overall, this study demonstrated a new method to tune optical and magnetic properties as well as showing how to grow unique microstructures.

Data availability

The data supporting this article have been included as part of the ESI.†

Author contributions

Conceptualization, investigation, methodology, writing—original draft, writing—review and editing, N. A. B.; investigation, writing-review and editing, L. Q., S. Z., A. G., A. C., Y. Z., J. S., and J. L.; funding acquisition, supervision, writing—review and editing, R. S. and A. S.; conceptualization, funding acquisition, supervision, writing—review and editing, H. W. All authors have read and agreed to the published version of the manuscript.

Conflicts of interest

The authors declare no conflicts of interest. The funders had no role in the design of the study; in the collection, analyses, or interpretation of data; in the writing of the manuscript, or in the decision to publish the results.

Acknowledgements

References

1 F. Franco-Martínez, C. Grasl, E. Kornfellner, M. Vostatek, A. M. Cendrero, F. Moscato and A. D. Lantada, Hybrid Design and Prototyping of Metamaterials and Metasurfaces, *Virtual Phys. Prototyp.*, 2022, **17**, 1031–1046, DOI: **10.1080/17452759.2022.2101009**.

2 L. Liu, L. Kang, T. S. Mayer and D. H. Werner, Hybrid Metamaterials for Electrically Triggered Multifunctional Control, *Nat. Commun.*, 2016, **7**, 13236, DOI: **10.1038/ncomms13236**.

3 A. Valipour, M. H. Kargozarfard, M. Rakhshi, A. Yaghootian and H. M. Sedighi, Metamaterials and Their Applications: An Overview, *Proc. Inst. Mech. Eng., Part L*, 2022, **236**, 2171–2210, DOI: **10.1177/1464420721995858**.

4 A. Chen and Q. Jia, A Pathway to Desired Functionalities in Vertically Aligned Nanocomposites and Related Architectures, *MRS Bull.*, 2021, **46**, 115–122, DOI: **10.1557/s43577-021-00032-4**.

5 S. Misra and H. Wang, Review on the Growth, Properties and Applications of Self-Assembled Oxide–Metal Vertically Aligned Nanocomposite Thin Films—Current and Future Perspectives, *Mater. Horiz.*, 2021, **8**, 869–884, DOI: **10.1039/D0MH01111H**.

6 D. Zhang, M. Kalaswad and H. Wang, Self-Assembled Vertically Aligned Nanocomposite Systems Integrated on Silicon Substrate: Progress and Future Perspectives, *J. Vac. Sci. Technol., A*, 2021, **40**, 010802, DOI: **10.1116/6.0001479**.

7 A. Chen, Z. Bi, Q. Jia, J. L. MacManus-Driscoll and H. Wang, Microstructure, Vertical Strain Control and Tunable Functionalities in Self-Assembled, Vertically Aligned Nanocomposite Thin Films, *Acta Mater.*, 2013, **61**, 2783–2792, DOI: **10.1016/j.actamat.2012.09.072**.

8 R. L. Paldi, X. Sun, X. Wang, X. Zhang and H. Wang, Strain-Driven In-Plane Ordering in Vertically Aligned ZnO–Au Nanocomposites with Highly Correlated Metamaterial Properties, *ACS Omega*, 2020, **5**(5), 2234–2241, DOI: **10.1021/acsomega.9b03356**.

9 N. A. Bhatt, R. L. Paldi, J. P. Barnard, J. Lu, Z. He, B. Yang, C. Shen, J. Song, R. Sarma, A. Siddiqui, *et al.*, ZnO-Au Hybrid Metamaterial Thin Films with Tunable Optical Properties, *Crystals*, 2024, **14**, 65, DOI: **10.3390/cryst14010065**.

10 R. L. Paldi, J. Lu, Y. Pachaury, Z. He, N. A. Bhatt, X. Zhang, A. El-Azab, A. Siddiqui and H. Wang, ZnO-AuxCu1−x Alloy and ZnO-AuxAl1−x Alloy Vertically Aligned Nanocomposites for Low-Loss Plasmonic Metamaterials, *Molecules*, 2022, **27**, 1785, DOI: **10.3390/molecules27061785**.

11 R. L. Paldi, X. Wang, X. Sun, Z. He, Z. Qi, X. Zhang and H. Wang, Vertically Aligned Ag x Au 1– x Alloyed Nanopillars Embedded in ZnO as Nanoengineered Low-Loss Hybrid Plasmonic Metamaterials, *Nano Lett.*, 2020, **20**, 3778–3785, DOI: **10.1021/acs.nanolett.0c00790**.

12 A. Chen, M. Weigand, Z. Bi, W. Zhang, X. Lü, P. Dowden, J. L. MacManus-Driscoll, H. Wang and Q. Jia, Evolution of Microstructure, Strain and Physical Properties in Oxide Nanocomposite Films, *Sci. Rep.*, 2014, **4**, 5426, DOI: **10.1038/srep05426**.

13 V. A. Owoeye, E. Ajenifuja, E. A. Adeoye, G. A. Osinkolu and A. P. Popoola, Microstructural and Optical Properties of Ni-Doped ZnO Thin Films Prepared by Chemical Spray Pyrolysis Technique, *Mater. Res. Express*, 2019, **6**, 086455, DOI: **10.1088/2053-1591/ab26d9**.

14 H. Ahmoum, G. Li, S. Belakry, M. Boughrara, M. S. Su'ait, M. Kerouad and Q. Wang, Structural, Morphological and Transport Properties of Ni Doped ZnO Thin Films Deposited by Thermal Co-Evaporation Method, *Mater. Sci. Semicond. Process.*, 2021, **123**, 105530, DOI: **10.1016/j.mssp.2020.105530**.

15 H. Ali, A. M. Alsmadi, B. Salameh, M. Mathai, M. Shatnawi, N. M. A. Hadia and E. M. M. Ibrahim, Influence of Nickel Doping on the Energy Band Gap, Luminescence, and Magnetic Order of Spray Deposited Nanostructured ZnO Thin Films, *J. Alloys Compd.*, 2020, **816**, 152538, DOI: **10.1016/j.jallcom.2019.152538**.

16 K. Natu, V. K. Kaushik and M. Laad, Optical and Structural Characterization of Aerosol-Assisted CVD-Grown Ni:ZnO Thin Films, *J. Korean Phys. Soc.*, 2023, **83**, 200–208, DOI: **10.1007/s40042-023-00809-7**.

17 P. Gupta and B. C. Joshi, Effect of Ni Incorporation on Structural, Optical, Morphological Properties of ZnO Thin Films Deposited by Laser Ablation, *J. Mater. Sci.: Mater. Electron.*, 2023, **34**, 1559, DOI: **10.1007/s10854-023-10985-8**.

18 J. Al Boukhari, A. Khalaf, R. Sayed Hassan and R. Awad, Structural, Optical and Magnetic Properties of Pure and Rare Earth-Doped NiO Nanoparticles, *Appl. Phys. A*, 2020, **126**, 323, DOI: **10.1007/s00339-020-03508-3**.

19 M. Khelil, S. Kraiem, K. Khirouni and S. Alaya, Growth of Crystalline Silicon by a Seed Layer Approach Using Plasma Enhanced Chemical Vapor Deposition, *Phys. B*, 2021, **609**, 412817, DOI: **10.1016/j.physb.2021.412817**.

20 Y. Singh, S. Rani, R. Parmar, R. Kumari, M. Kumar, B. Sairam, A. Mamta and V. N. Singh, Sb2Se3 Heterostructure Solar Cells: Techniques to Improve Efficiency, *Sol. Energy*, 2023, **249**, 174–182, DOI: **10.1016/j.solener.2022.11.033**.

21 S. Nikodemski, A. A. Dameron, J. D. Perkins, R. P. O'Hayre, D. S. Ginley and J. J. Berry, The Role of Nanoscale Seed Layers on the Enhanced Performance of Niobium Doped TiO2 Thin Films on Glass, *Sci. Rep.*, 2016, **6**, 32830, DOI: **10.1038/srep32830**.

22 J.-T. Luo, A.-J. Quan, Z.-H. Zheng, G.-X. Liang, F. Li, A.-H. Zhong, H.-L. Ma, X.-H. Zhang and P. Fan, Study on the Growth of Al-Doped ZnO Thin Films with (1120) and (0002) Preferential Orientations and Their Thermoelectric Characteristics, *RSC Adv.*, 2018, **8**, 6063–6068, DOI: **10.1039/C7RA12485F**.

23 K. Vijayalakshmi, K. Karthick and K. Tamilarasan, Enhanced H2 Sensing Properties of A-Plane ZnO Prepared on c-Cut Sapphire Substrate by Sputtering, *J. Mater. Sci.: Mater. Electron.*, 2013, **24**, 1325–1331, DOI: **10.1007/s10854-012-0927-y**.

24 J. Huang, X. L. Phuah, L. M. McClintock, P. Padmanabhan, K. S. N. Vikrant, H. Wang, D. Zhang, H. Wang, P. Lu, X. Gao, *et al.*, Core-Shell Metallic Alloy Nanopillars-in-Dielectric Hybrid Metamaterials with Magneto-Plasmonic Coupling, *Mater. Today*, 2021, **51**, 39–47, DOI: **10.1016/j.mattod.2021.10.024**.

25 R. L. Paldi, M. Kalaswad, J. Lu, J. P. Barnard, N. A. Richter, M. Si, N. A. Bhatt, P. D. Ye, R. Sarma, A. Siddiqui, *et al.*, ZnO–Ferromagnetic Metal Vertically Aligned Nanocomposite Thin Films for Magnetic, Optical and Acoustic Metamaterials, *Nanoscale Adv.*, 2023, **5**, 247–254, DOI: **10.1039/D2NA00444E**.

26 I. O. Kruhlov, A. K. Orlov, O. Dubikovskyi, Y. Iguchi, Z. Erdélyi, S. I. Sidorenko, T. Ishikawa, S. V. Prikhodko and S. M. Voloshko, Inhibition of Interlayer Diffusion and Reduction of Impurities in Thin Metal Films by Ion

Irradiation, *Mater. Today Commun.*, 2023, **34**, 104977, DOI: **10.1016/j.mtcomm.2022.104977**.

27 J. Huang, Z. Qi, L. Li, H. Wang, S. Xue, B. Zhang, X. Zhang and H. Wang, Self-Assembled Vertically Aligned Ni Nanopillars in CeO2 with Anisotropic Magnetic and Transport Properties for Energy Applications, *Nanoscale*, 2018, **10**, 17182–17188, DOI: **10.1039/C8NR05532G**.

28 Q. Su, W. Zhang, P. Lu, S. Fang, F. Khatkhatay, J. Jian, L. Li, F. Chen, X. Zhang, J. L. MacManus-Driscoll, *et al.*, Self-Assembled Magnetic Metallic Nanopillars in Ceramic Matrix with Anisotropic Magnetic and Electrical Transport Properties, *ACS Appl. Mater. Interfaces*, 2016, **8**, 20283–20291, DOI: **10.1021/acsami.6b05999**.

29 D. Rathore, M. Garayt, Y. Liu, C. Geng, M. Johnson, J. R. Dahn and C. Yang, Preventing Interdiffusion during Synthesis of Ni-Rich Core–Shell Cathode Materials, *ACS Energy Lett.*, 2022, **7**, 2189–2195, DOI: **10.1021/acsenergylett.2c01009**.

30 S. Kok, Y. Go, X. Wang and D. Wong, A Review of Nanostructure Coating Techniques to Achieve High-Precision Optical Fiber Sensing Applications, *Nanomanufacturing*, 2024, **4**, 214–240, DOI: **10.3390/nanomanufacturing4040015**.

31 K. Li, R. Tang, C. Zhu and T. Chen, Critical Review on Crystal Orientation Engineering of Antimony Chalcogenide Thin Film for Solar Cell Applications, *Advanced Science*, 2024, **11**, 2304963, DOI: **10.1002/advs.202304963**.

32 Y. Kim, Y. Choi, S. A. Lee, W. S. Choi and K. T. Kang, Complex Oxide Thin Films: A Review on Pulsed Laser Epitaxy Growth, *Curr. Appl. Phys.*, 2024, **68**, 113–130, DOI: **10.1016/j.cap.2024.09.001**.

33 H.-W. Yu, M. J. Halonen and I. L. Pepper, Chapter 12 - Immunological Methods, in *Environmental Microbiology*, ed. I. L. Pepper, C. P. Gerba and T. J. Gentry, Academic Press, San Diego, 3rd edn, 2015, pp. 245–269 ISBN 978-0-12-394626-3.

34 K.-L. Zhang, Z.-L. Hou, L.-B. Kong, H.-M. Fang and K.-T. Zhan, Origin of Negative Imaginary Part of Effective Permittivity of Passive Materials, *Chinese Phys. Lett.*, 2017, **34**, 097701, DOI: **10.1088/0256-307X/34/9/097701**.

35 K. M. Mayer and J. H. Hafner, Localized Surface Plasmon Resonance Sensors, *Chem. Rev.*, 2011, **111**, 3828–3857, DOI: **10.1021/cr100313v**.

36 N. Fitria, M. Sujak and D. Djuhana, The Influence of Gap Spacing in Localized Surface Plasmon Resonance (LSPR) Spectra of Ag Nanorod-Coupled with End-to-End Assembly Using Boundary Element Method, *IOP Conf. Ser.: Mater. Sci. Eng.*, 2020, **763**, 012062, DOI: **10.1088/1757-899X/763/1/012062**.

37 L. Ferrari, C. Wu, D. Lepage, X. Zhang and Z. Liu, Hyperbolic Metamaterials and Their Applications, *Prog. Quant. Electron.*, 2015, **40**, 1–40, DOI: **10.1016/j.pquantelec.2014.10.001**.

38 K. Maaz, A. Mumtaz, S. K. Hasanain and M. F. Bertino, Temperature Dependent Coercivity and Magnetization of Nickel Ferrite Nanoparticles, *J. Magn. Magn. Mater.*, 2010, **322**, 2199–2202, DOI: **10.1016/j.jmmm.2010.02.010**.

39 G. A. Landrum and R. Dronskowski, The Orbital Origins of Magnetism: From Atoms to Molecules to Ferromagnetic Alloys, *Angew. Chem., Int. Ed.*, 2000, **39**, 1560–1585, DOI: **10.1002/(SICI)1521-3773(20000502)39:9<1560::AID-ANIE1560>3.0.CO;2-T**.

40 R. Singh, Unexpected Magnetism in Nanomaterials, *J. Magn. Magn. Mater.*, 2013, **346**, 58–73, DOI: **10.1016/j.jmmm.2013.07.005**.

41 M. Zargar Shoushtari, A. Poormoghadam and M. Farbod, The Size Dependence of the Magnetic Properties of ZnO and Zn1-xNixO Nanoparticles, *Mater. Res. Bull.*, 2017, **88**, 315–319, DOI: **10.1016/j.materresbull.2017.01.006**.

42 S. Harke, A. Habibpourmoghadam, A. B. Evlyukhin, A. Calà Lesina and B. N. Chichkov, Low-Frequency Magnetic Response of Gold Nanoparticles, *Sci. Rep.*, 2023, **13**, 21588, DOI: **10.1038/s41598-023-48813-y**.

43 S. D. Tiwari and K. P. Rajeev, Magnetic Properties of NiO Nanoparticles, *Thin Solid Films*, 2006, **505**, 113–117, DOI: **10.1016/j.tsf.2005.10.019**.

44 N. Sarmadi, F. Pahlevani, S. Udayakumar, S. Biswal, M. F. Pervez, C. Ulrich, A. Chakraborty, S. K. Bhattacharyya and V. Sahajwalla, Correlative Analysis of Microstructural and Magnetic Characteristics of Dual-Phase High-Carbon Steel, *Adv. Eng. Mater.*, 2024, **26**, 2300826, DOI: **10.1002/adem.202300826**.

45 G. E. Fish, Soft Magnetic Materials, *Proc. IEEE*, 1990, **78**, 947–972, DOI: **10.1109/5.56909**.

46 B. X. Rutherford, D. Zhang, L. Quigley, J. P. Barnard, B. Yang, J. Lu, S. Kunwar, H. Dou, J. Shen, A. Chen, *et al.*, Combinatorial Growth of Vertically Aligned Nanocomposite Thin Films for Accelerated Exploration in Composition Variation, *Small Science*, 2023, **3**, 2300049, DOI: **10.1002/smsc.202300049**.